Pacific Northwest
NATIONAL LABORATORY

PNNL-34957 Rev 0
DVZ-RPT-093 Rev 0

Joint Inversion of Surface Electrical Resistivity Tomography and Seismic Refraction Data between the 200 Areas

September 2023

James St. Clair
Judith Robinson
Timothy Johnson

U.S. DEPARTMENT OF ENERGY

Prepared for the U.S. Department of Energy
under Contract DE-AC05-76RL01830

DISCLAIMER

PACIFIC NORTHWEST NATIONAL LABORATORY
operated by
BATTELLE
for the
UNITED STATES DEPARTMENT OF ENERGY
under Contract DE-AC05-76RL01830

Printed in the United States of America

Available to DOE and DOE contractors from the
Office of Scientific and Technical Information,
P.O. Box 62, Oak Ridge, TN 37831-0062;
ph: (865) 576-8401
fax: (865) 576-5728
email: reports@adonis.osti.gov

Available to the public from the National Technical Information Service
5301 Shawnee Rd., Alexandria, VA 22312
ph: (800) 553-NTIS (6847)
email: orders@ntis.gov <https://www.ntis.gov/about>
Online ordering: http://www.ntis.gov

PNNL-34957 Rev 0
DVZ-RPT-093 Rev 0

Joint Inversion of Surface Electrical Resistivity Tomography and Seismic Refraction Data between the 200 Areas

September 2023

James St. Clair
Judith Robinson
Timothy Johnson

Prepared for
the U.S. Department of Energy
under Contract DE-AC05-76RL01830

Pacific Northwest National Laboratory
Richland, Washington 99354

Summary

Geologic stratigraphy on the Hanford Site influences groundwater and contaminant migration through the aquifer system and the vadose zone. The current geologic framework model (GFM) relies heavily on a sparse distribution of borehole data in some locations to map geologic contacts and hydrologic properties in the subsurface. Non-invasive geophysical methods such as electrical resistivity tomography (ERT), transient electromagnetic surveying, and seismic imaging are being used at Hanford to map subsurface structure in areas with limited well observations. This is to develop and mature the capability of geophysical methods to aid in GFM refinement, to identify regions of subsurface complexity, and for optimal well siting.

A joint inversion of co-located seismic refraction and ERT data was carried out for data collected on a ~2.3-km profile between the 200 Areas on the Hanford Site. While ERT and seismic refraction images have sensitivity to overlapping physical properties (porosity, moisture content, lithology), the resolution and physics used to acquire each of these datasets are different and therefore information can be different or mutually complementary. Performing a joint inversion provides a reasonable option for a coherent, coupled interpretation for mutually complementary datasets. Between the 200 Areas, there are few boreholes to interpret the geologic framework model, and these data sets were obtained to provide a first line of evidence toward identifying stratigraphic structure. The seismic refraction and ERT data were independently inverted during fiscal year 2022 and broadly showed a two-layer structure with a trough-like feature that is ~1 km wide and upwards of 150 m deep. The depth of the trough feature was greater in the ERT image compared to the seismic image, which indicated a maximum depth of approximately 110 m.

The objective of the joint inversion described in this report was to invert the seismic refraction and ERT data together while constraining the ERT image to be structurally similar to the seismic refraction image. The approach was applied using the geophysical inverse modeling program E4D, which has the capability to invert first-arrival times from seismic refraction data and ERT resistances using a “cross-gradient” constraint. The application of cross-gradient constraints with different weights produces ERT models that show a high degree of similarity within the upper 100 m (above ~120 m elevation). None of the ERT models show an improved structural similarity to the seismic result; therefore, it is recommended that further attempts to jointly interpret these models focus on petrophysics and image resolution. Petrophysical measurements of core samples would improve knowledge of what drives the ERT response in this region and, along with downhole geophysical measurements, could be used to “ground truth” the surface-based geophysical results. Image resolution studies would provide insight into which regions of the inverted images are reliable and which regions are poorly constrained.

Acknowledgments

This document was prepared by the Deep Vadose Zone - Applied Field Research Initiative at Pacific Northwest National Laboratory. Funding for this work was provided by the U.S. Department of Energy (DOE) Richland Operations Office. The Pacific Northwest National Laboratory is operated by Battelle Memorial Institute for the DOE under Contract DE-AC05-76RL0183.

Acronyms and Abbreviations

2D	two-dimensional
3D	three-dimensional
E4D	geophysical modeling and inversion software
EC	electrical conductivity
ERT	electrical resistivity tomography
GFM	geological framework model
MISC	seismic refraction tomography inversion code
Vp	seismic compressional wave velocity

Contents

Figures

1.0 Introduction

Geologic stratigraphy on the Hanford Site influences groundwater and contaminant migration through the aquifer system and the vadose zone. The current geologic framework model (GFM) relies heavily on a sparse distribution of wells in some locations to map geologic contacts and hydrologic properties in the subsurface. Non-invasive geophysical methods such as electrical resistivity tomography (ERT), transient electromagnetic surveying, and seismic imaging are being used at Hanford to map subsurface structure in areas with limited well observations. This is to develop and mature the capability of geophysical methods to aid in GFM refinement, to identify regions of subsurface complexity, and for optimal well siting.

Recently, 10 quasi-parallel ERT profiles were collected in-between the 200 East and 200 West areas on the Hanford Site's Central Plateau (Robinson et al. 2023; Robinson et al. 2022; Robinson et al. 2020). The goal of these ERT surveys was to investigate the possibility of a preferential groundwater flow pathway, a paleochannel, in the area where contaminants could more rapidly be transported. Two-dimensional (2D) and quasi-three-dimensional (3D) inversions of this data broadly showed a low bulk electrical conductivity (EC) layer overlying a layer with higher EC. A channel-like low bulk EC region with a northwest to southeast orientation was observed in the eastern part of the study area. This agreed with the location of a hypothesized paleochannel however the feature imaged strikes to NNW to SSE in contrast to the conceptual model of this location, which hypothesizes an E-W oriented channel. There are few boreholes to validate these findings. Therefore, in fiscal year 2022, 2D seismic refraction surveys were conducted along two of the ERT profiles and seismic refraction inversion images were compared to the ERT images. The seismic refraction images displayed some similarities to the ERT images; however, the channel-like feature was shallower in the seismic result.

While ERT and seismic refraction images have sensitivity to overlapping physical properties (porosity, moisture content, lithology), the resolution and physics used to acquire each of these datasets are different and therefore information can be different or mutually complementary. Performing a joint inversion provides a reasonable option for a coherent, coupled interpretation for mutually complementary datasets. In a joint inversion, two datasets (in this case, ERT and seismic refraction) are simultaneously inverted to recover model images. This can be done by constraining the model solutions using a known relationship between the geophysical parameters, or through structural constraints that are defined through a spatial coincidence of boundaries or transition zones (Haber and Oldenburg 1997). Since structural similarities were evident in the ERT and seismic refraction images, a joint inversion using a structural constraint was deemed to be a reasonable approach. The cross-gradient approach (Jordi 2020) is commonly used to apply these structural constraints, which is where the inversion attempts to minimize the structural differences between the ERT and seismic refraction model images.

The purpose of this report was to expand on the independent interpretations and analyses of ERT and seismic refraction tomography data (Robinson et al. 2023) by jointly inverting coincident geophysical data along one profile to better understand complementary dataset information. A 3D parallel joint inversion capability using cross-gradient constraints (Zhu et al. 2020) was recently added to the geophysical and modeling software E4D (Johnson 2014; Johnson et al. 2010). This new module was used to investigate whether a joint inversion could be used to interpret ERT and seismic refraction tomography model images, and this is the first time that E4D has been used to jointly invert surface-based field data.

This report is organized to first briefly introduce the geophysical methods, including data acquisition, image resolution, processing, and a description of cross-gradient constraints. This is followed by a summary of results from previous work where each geophysical survey was individually processed. Next, results of the joint inversion are presented, which show the impact of using different weights on the cross-gradient constraint. We show that the weighting used in the cross-gradient constraint must be large relative to the data and model weighting. This is because the bulk EC and slowness gradients within the

ERT and seismic models are predominantly vertical, parallel to one another or very close to zero, causing the cross-gradient terms to be very small. We present two jointly inverted ERT models where different weighting is used for the cross-gradient constraint. While these jointly inverted ERT models statistically fit the data equally well, their bulk EC structures are different below elevations of ~125 m (depths greater than ~90-100 m), demonstrating the reduced sensitivity of the ERT data with depth. We therefore found that in this site-specific scenario where there are small cross-gradients, use of structural constraints has limited utility because of the sensitivity (and subjectivity) to the weighting term. Other approaches to jointly analyze these datasets could include a systematic study of image resolution, a petrophysical-based joint inversion, or geostatistical methods.

2.0 Site Location

Figure 1 shows the location of the co-located ERT and seismic profiles. This report focuses on Line 4. Line 4 is an approximately 2.3-km-long profile between the 200 Areas that was chosen for the joint inversion.

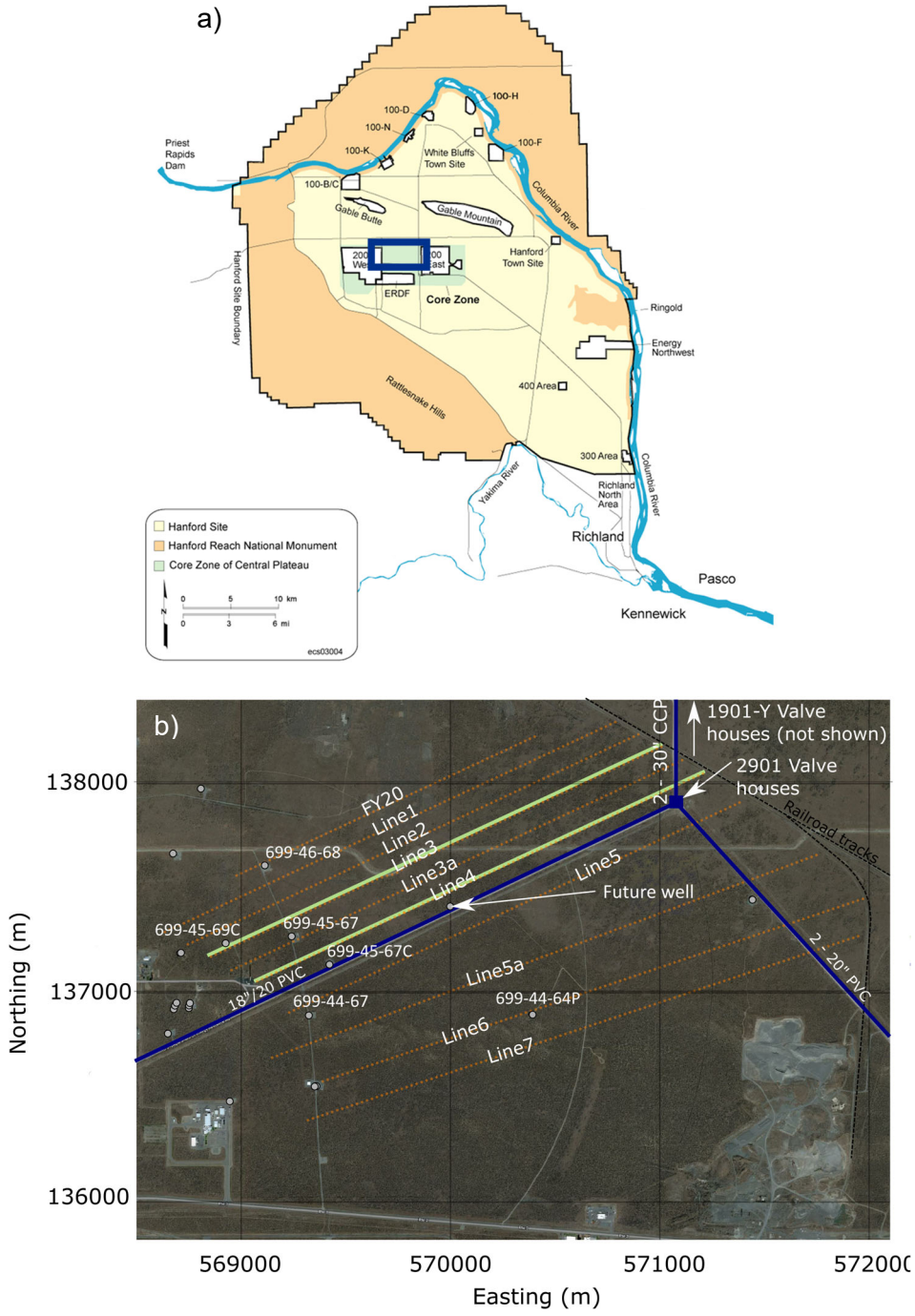

Figure 1. a) The location of ERT and seismic profiles on the Hanford Site (blue rectangle) b) ERT (electrode locations shown as orange circles) and coincident seismic refraction profiles (green) on Lines 3 and 4 between the 200 Areas. This report focuses on Line 4.

3.0 Methods

This section provides an overview of ERT and seismic refraction tomography methods. For additional information and details related to this field campaign, refer to Robinson et al. (2023).

3.0 Electrical Resistivity Tomography

Electrical resistivity (the inverse of EC) is a physical property of the subsurface that quantifies how strongly a material opposes the flow of an electrical current. This is controlled by porosity, moisture content, temperature, pore water fluid conductivity, and soil texture (Archie 1942). ERT is an active source geophysical method that uses an array of electrodes to image subsurface bulk EC. Data is collected by inserting sensors, called electrodes, into the ground and injecting a direct current (I) between two electrodes and then measuring the voltage drop (ΔV) between two other receiving electrodes. The basic unit of ERT data is transfer resistance (ohm), which is the measured voltage drop (ΔV) across the receiving electrodes divided by the injected current (I).

The spatial resolution and volume of interrogation of ERT measurements is governed by several factors, including the electrode spacing and orientation/configuration. Electrodes with spacings that are farther apart sample a larger volume with lower spatial resolution. In comparison, closer-spaced electrodes sample a smaller volume with higher spatial resolution. Two common electrode orientations are typically used: (1) nested arrays, which is where the current electrodes surround the potential electrodes; and (2) dipole arrays, which is where the current electrodes are adjacent to the potential electrodes. Generally, nested arrays have a higher signal-to-noise ratio and tend to image vertical structure better than dipole arrays. Dipole arrays tend to image lateral variations better than nested arrays (Binley and Slater 2020). These general spacing and orientation principles were used in the ERT survey design for this field campaign to optimally resolve targeted subsurface locations.

The ERT survey was designed to image to depths of 50-150 m below ground surface and potentially deeper. The electrodes spacing was 25 m and electrode survey geometries included dipole-dipole, Wenner, Schlumberger, and multiple gradient (Robinson et al. 2022). To solve for subsurface spatial distributions of bulk EC, ERT data of resistance values was analyzed using E4D (Johnson 2014). ERT imaging resolution is governed by many factors, including electrode spacing, proximity to electrodes, background electrical noise, and measurement sequence. E4D generates an approximate sensitivity map indicating the relative sensitivity of the data misfit to each model parameter. For the 2D ERT imaging collected here, the highest image resolution is directly beneath the line, with higher resolution closer to the surface, decreasing with depth. ERT images will be shown as 2D slices with areas of lower normalized sensitivity (e.g., relative sensitivity normalized by mesh element volume) grayed out, so that these regions are not over-interpreted (Johnson and Wellman 2015).

3.1 Seismic Refraction Tomography

Seismic refraction surveys measure the propagation of elastic waves in the subsurface and allow for estimates of the compressional (Vp) velocities. These velocities are sensitive to lithology, porosity, confining pressure, and moisture content. Previous work measuring Vp at the Hanford Site (Rohay and Brouns 2007; Redpath 2007; Linneman et al. 2021; Hyde et al. 2011) suggests that Vp can reliably differentiate the Hanford and Cold Creek Units from the Ringold Formation and Basalt group [refer to Rohay and Brouns (2007), for Hanford stratigraphic column].

Seismic refraction data is obtained using geophones, a seismograph, and an impulsive source. Geophones are essentially a magnet inside a coil. Ground motion causes the magnet to move with respect to the coil

and a voltage is induced that is proportional to the ground motion produced by the wave front. An impulsive source is needed to generate the wavefield and the seismograph digitizes the electrical signal generated by the ground motion. Signal to noise is increased by stacking successive shots. With stacking, repeatable signals are enhanced, while background noise tends to cancel out.

The seismic refraction method depends on increasing Vp with depth and uses the travel times of the first arriving energy propagated from a seismic source. First arrival times depend on the subsurface Vp distribution. For a simple, layered Vp model, part of the wavefield travels directly along the surface to the geophones; this is called the "direct wave." Measuring the arrival time of the direct wave at each geophone yields a line whose slope is 1/Vp. When the downward propagating seismic wave encounters a boundary where Vp increases, it will bend (or refract) toward the horizontal direction. If it encounters a lower Vp, it will bend toward the vertical direction. The change in angle depends on the Vp contrast and the incidence angle. At a certain incidence angle, called the "critical angle," the wave will turn horizontal and radiate energy back toward the surface; this is called the "refracted head wave." At some distance from the source, it will take the refracted wave less time to reach the geophones than the direct wave and the refracted wave will become the first arrival. This description allows for explanation of a key point: In order to see deep seismic boundaries, the geophones must be far enough away from the source for the refracted wave to become the first arrival. This offset distance depends on the Vp contrast and the depth to the refracting boundary. Thus, the depth of investigation for the seismic refraction method depends on the subsurface Vp structure and the distance between the sources and geophones. Generally, longer offsets are required to image deeper seismic structure.

The seismic refraction data was recorded on a 96-channel Geometrics Geode system. A sledgehammer striking a steel plate was used as the source. Geophone spacing was 5 m and shot spacing was also 5 m. Source-geophone offsets range between 2.5 and at least 250 m, the maximum offset was 475 m. The survey was optimized for reflection, refraction, and multichannel analysis of shear waves; however, this report focuses on the compressional wave (Vp) images from the seismic refraction tomography.

Manually interpreted first-arrival travel times were initially inverted with the travel-time inversion module of E4D. However, a satisfactory model could not be found. Instead, the 2D tomography code Miscellaneous Inverse Seismic Codes (MISC), written in MATLAB (St. Clair 2015), was used to produce a Vp image. This code parameterizes the subsurface as a large number of parallelograms of constant Vp. The vertical dimension of these cells increases linearly with depth, while the horizontal dimension is held fixed throughout the model. For the models in this report, the horizontal dimension is 2.5 m and the vertical dimension increases linearly from 2.5 to 5 m over an interval of 150 m. Travel times are predicted using the shortest path algorithm (Dijkstra 1959; Moser 1991). The chosen regularization strategy is one that allows some sharp boundaries while attempting to keep vertical and lateral gradients at zero everywhere else. This approach was chosen because it is known *a priori* that there is a sharp Vp contrast between the Hanford sediments and all other stratigraphic units likely to be present [e.g. (Rohay and Brouns 2007); St. Clair et al. (2023)].

3.2 ERT and Seismic Travel-Time Inversions in E4D

E4D is an open-source finite element code designed specifically to run on distributed-memory, parallel, high-performance computing systems. A flexible set of inputs allows the geophysical analysis to include site-specific information, which can be incorporated in the finite element mesh or used as constraints on the model solution. Constraints can result in improved imaging resolution to obtain a physically realistic interpretation. E4D can invert for bulk EC or Vp using ERT resistances or seismic first arrival times, respectively. The following objective function (Φ_t) is minimized, which is the sum of data misfit (Φ_d) and model misfit (Φ_m).

$$\Phi_t = \Phi_d + \beta\Phi_m \quad (1)$$

In Eq. (1), Φ_d minimizes the difference between the predicted and observed data, subject to data weighting; Φ_m minimizes model misfit, subject to weighting functions and structural metrics defined within the E4D framework; and β controls the relative importance of the data fit and the model constraints. Refer to Johnson et al. (2010) for more details.

In the joint inversion implementation within E4D, ERT resistances and seismic first-arrival travel times are used as inputs to solve for a bulk EC and Vp. Φ_t contains an additional cross-gradient (Φ_{cg}) term:

$$\Phi_t = \Phi_d + \beta\Phi_m + \lambda\Phi_{cg} \quad (2)$$

In the joint inversion objective function, Φ_{cg} minimizes the cross product of two gradient vectors, which provides an element-to-element measure of the structural differences between bulk EC and Vp. The minimization of Φ_{cg} encourages structural similarity by penalizing differences in the model gradient vectors. λ controls the overall weighting/tradeoff of this term in the objective function. For additional information and details, refer to Zhu et al. (2020).

Figure 2 depicts the application of cross-gradient constraints used in Φ_{cg}. In panel A, two models ($\boldsymbol{m_A}$ and $\boldsymbol{m_B}$) have gradient vectors that are parallel and their cross-gradient (**t**) is zero. In panel B, the two models have gradient vectors that are anti-parallel and their cross-gradient is zero. In panel C, $\boldsymbol{m_B}$ has zero gradient and the cross-gradient term is again zero. Finally, in panel D, the two models have perpendicular gradient vectors and the cross-gradient term is non-zero. More generally, the cross-gradient term can be understood by inspecting the following equation:

$$\boldsymbol{t} = \|\boldsymbol{m_A}\|\|\boldsymbol{m_B}\| sin\theta \quad (3)$$

where **t** is the cross-gradient, $\boldsymbol{m_A}$ and $\boldsymbol{m_B}$ are the gradient vectors, and θ is the angle between them. The magnitude of **t** depends on the magnitudes of the gradient vectors as well as the angle between them.

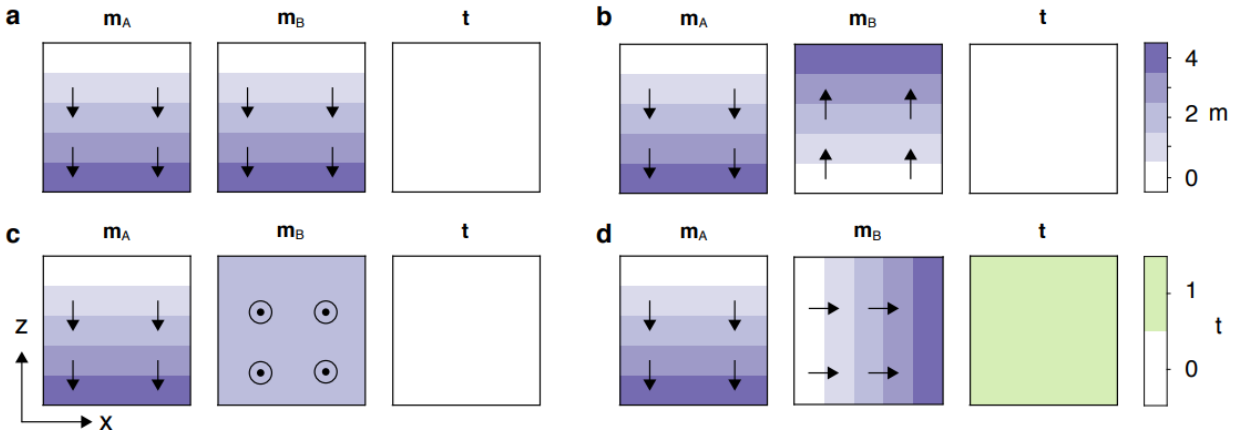

Figure 2. Cross-gradient constraint after Jordi (2020). (a) Models A ($\boldsymbol{m_A}$) and B ($\boldsymbol{m_B}$) have gradient vectors (shown as black arrows) pointing in same direction and the cross gradient (t) = 0. (b) $\boldsymbol{m_A}$ and $\boldsymbol{m_B}$ have gradient vectors pointing in opposite, parallel directions and t = 0. (c) $\boldsymbol{m_B}$ has a zero gradient vector and t = 0. (d) $\boldsymbol{m_A}$ and $\boldsymbol{m_B}$ have gradient vectors that are perpendicular and t > 0.

The cross-gradient constraint in E4D (Zhu et al. 2020) seeks to find a Vp and a bulk EC that both change in a similar way. That is, it seeks a model for the bulk EC and Vp with gradient vectors that point in the same direction. How strongly it can enforce this constraint depends on the magnitude of the respective gradient vectors, the angle between them, and how Φ_{cg} is weighted with respect to Φ_d and Φ_m. In our implementation, we used the cross-gradient constraint to seek a bulk EC with a similar structure as the Vp solution from MISC. This was achieved by minimizing updates to Vp during the joint inversion by imposing a penalty within Φ_m for deviations from the starting model.

Since the 2D Vp result from MISC was used as the starting model within the joint inversion, it needed to be extrapolated to the 3D model domain used for ERT in E4D. This was achieved by rotating the ERT model domain so that the geophone locations were parallel to the x-axis and in the 2D plane used by MISC. Since the surface extent and depth of the ERT model domain were larger than in the MISC model domain, the 2D Vp model was expanded on each side and at depth so that Vp values were defined for the entire model domain. The expansion assumed that there was no structural change between the edges of the 2D model domain and the edges of the 3D model domain. Then, the 2D Vp was interpolated onto the x-z coordinates of the rotated 3D model domain. Finally, the 3D model domain was rotated back to its original position.

Model constraints for the ERT inversion (Φ_m) were chosen to minimize the bulk EC difference between neighboring mesh elements with a preference for smoother structure in the horizontal direction than in the vertical direction. A β value of 100 was chosen with the option for reducing β by 50% if the overall objective function decreases by less than 5% after an iteration. For the Φ_{cg} term, λ values of 1e7 and 1e9 were chosen. The large λ values compared to β means that the cross-gradient term should have more influence on the objective function than the data and model terms, subject to the magnitude of the cross-gradients as computed in Eq. (3). This λ value was chosen after a few trials where it was clear that the Φ_{cg} term was small compared to the other terms in the objective function.

4.0 Results

4.0 Independent Geophysical Images

Figure 3 shows the independently inverted ERT and seismic refraction data. The ERT image (Figure 3, top) is shown with a grayed-out area at depth to indicate the region with a lower normalized sensitivity, which is where there is higher uncertainty in the image. The ERT results show a similar structure when compared to the seismic image results (Figure 3, bottom). The ERT results indicate a low bulk EC layer over a high bulk EC layer with a low EC trough between model distances 1000 and 1900 m. The seismic Vp image indicates a low Vp layer over a high Vp layer with a sharp transition between 800- and 2100-m distance. The depth at which there is a contrast in bulk EC is deeper than shown for the contrast in Vp, although it is unclear how well this boundary is resolved by the ERT data. The boundary between 800 and 2100 m is well resolved by the seismic data. The goal of the joint inversion is to search the bulk EC model space for a solution that agrees with the observed data and is more structurally similar to the Vp result.

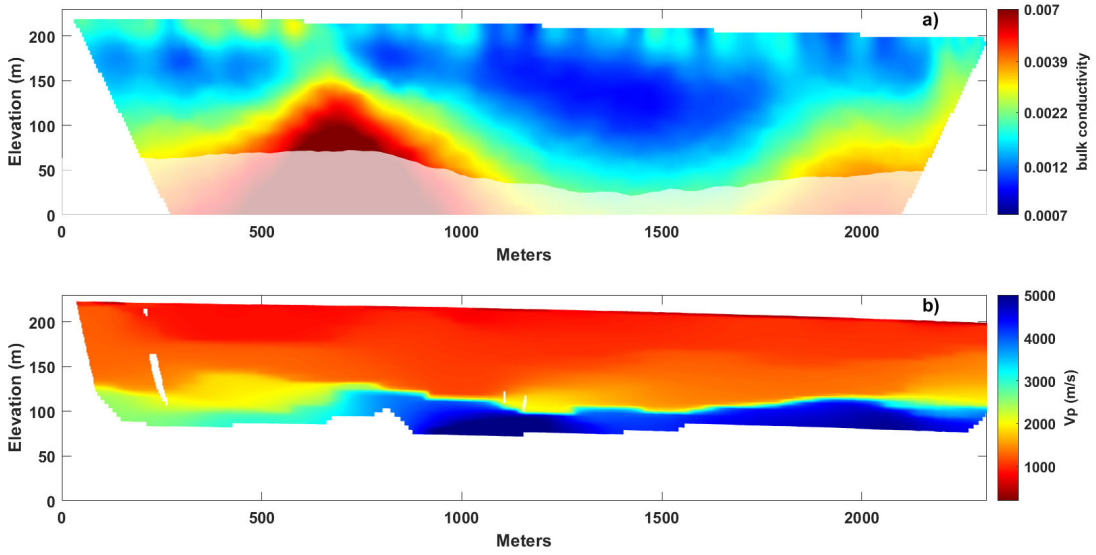

Figure 3. Independent inversions for Line 4 (for location, see Figure 2) of ERT and seismic refraction data shown as (a) bulk EC and (b) Vp. Grayed out areas in the ERT image indicate regions with lower normalized sensitivity.

4.1 Joint Inversion Results

Figure 4 shows the joint ERT inversion results with the independent ERT and seismic inversions for comparison. The jointly inverted ERT result with λ=1e7 shows a weak boundary that is coincident with the transition from slow (Vp < 2500 m/s) to fast (Vp > 4000 m/s) seismic velocities. However, the deeper low-conductivity trough is still evident as are the more conductive zones to each side of it. The jointly inverted ERT result with λ=1e9 shows a slight increase in bulk EC that is coincident with the seismic transition and the low-conductivity trough is not evident. This result shows two conductive bodies: one between 500 and 800 m and the other at greater than 2100 m along the profile.

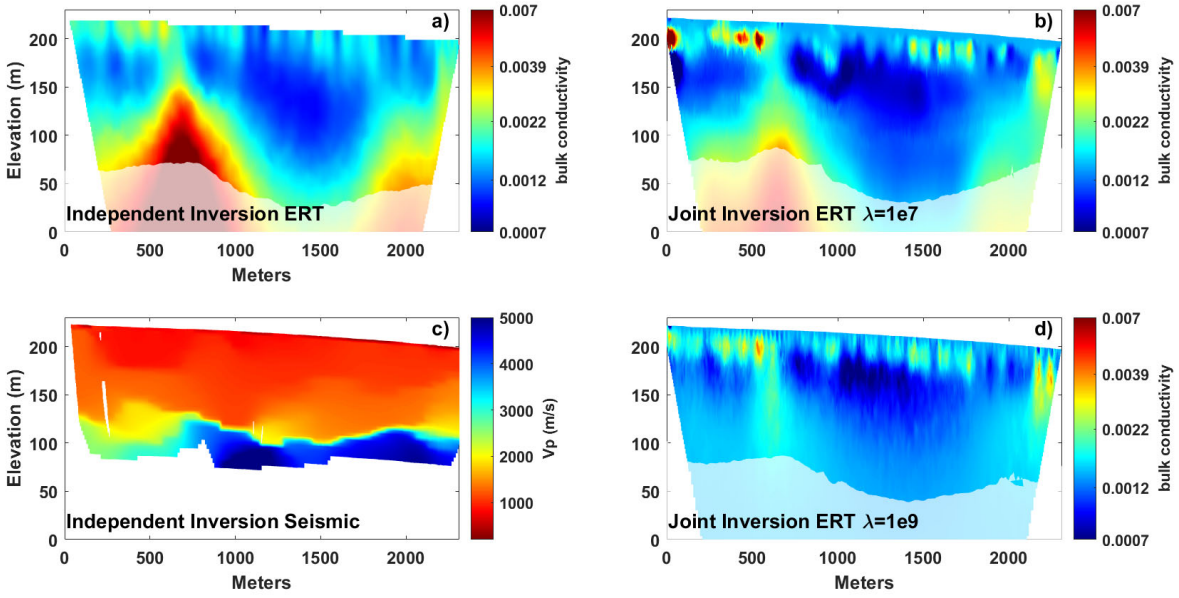

Figure 4. Line 4 inversion results: (a) independent ERT inversion, (b) joint ERT inversion with λ=1e7, and (d) joint ERT inversion with λ=1e9. Grayed out areas in the ERT images indicate regions with lower normalized sensitivity. The independent seismic inversion is shown in (c) for comparison.

Plots of the x and z components of the gradient vectors for the independently inverted Vp and bulk EC images illustrate the impact of the cross-gradient terms on the inverted ERT structure (Figure 5) without considering the value of λ. The seismic gradients are computed from slowness (1/Vp), since the inversion in E4D is parameterized as slowness, and are mostly zero in the x and z directions except where there are strong vertical changes in slowness. In both the seismic and ERT images, the absolute gradients are largest in the vertical direction, which means that the independently inverted results are already somewhat structurally similar as defined by the cross-gradient. Note that in areas where the seismic gradient is large (i.e., at a boundary), if the ERT gradient at that location is parallel to the higher seismic gradient, the cross-gradient term will be zero and will have no influence on the joint inversion image.

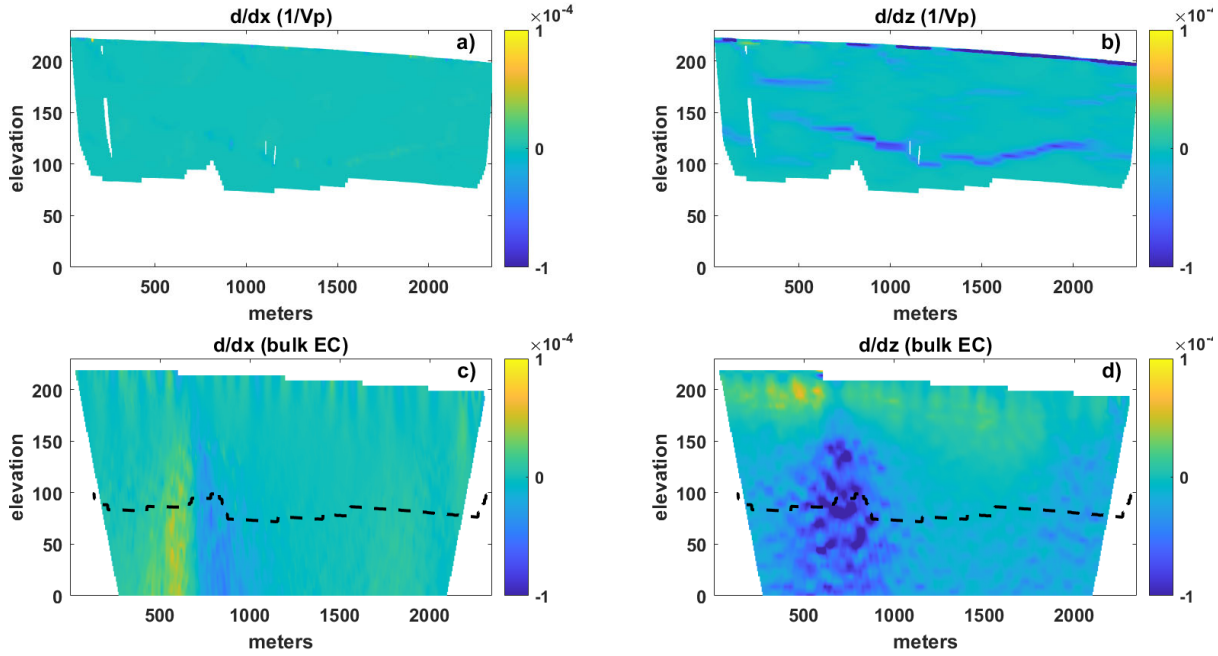

Figure 5. Vp (a and b) and bulk EC (c and d) x and z gradients for the independently inverted models shown in Figure 3. Dashed lines in bulk EC gradients indicate the lower limit of the seismic model. Seismic gradients are computed from the slowness (1/Vp).

The behavior of each objective function term at each iteration of the inversion illustrates the impact of the cross-gradient term when λ=1e7 (Figure 5a). After the first iteration, the cross-gradient term is relatively small because there is very little structure in the first solution. At the second iteration, the cross-gradient term is large compared to the data and model terms. By the third iteration, the cross-gradient term is again very small compared to the data and model terms and it continues to decrease at each iteration. Thus, for this choice in λ, the joint ERT inversion is highly similar to the independent ERT inversion. In contrast, when λ=1e9 (Figure 6b), the cross-gradient term starts out large and continues to grow with each iteration. In fact, the cross-gradient term is the largest term in the objective function throughout the inversion. For this choice of λ, the joint ERT inversion is less similar to the independent inversion than for λ=1e7. The cross-gradient for the final ERT solution at λ=1e9 is very large, indicating that the structure for this model is not similar to the seismic model either.

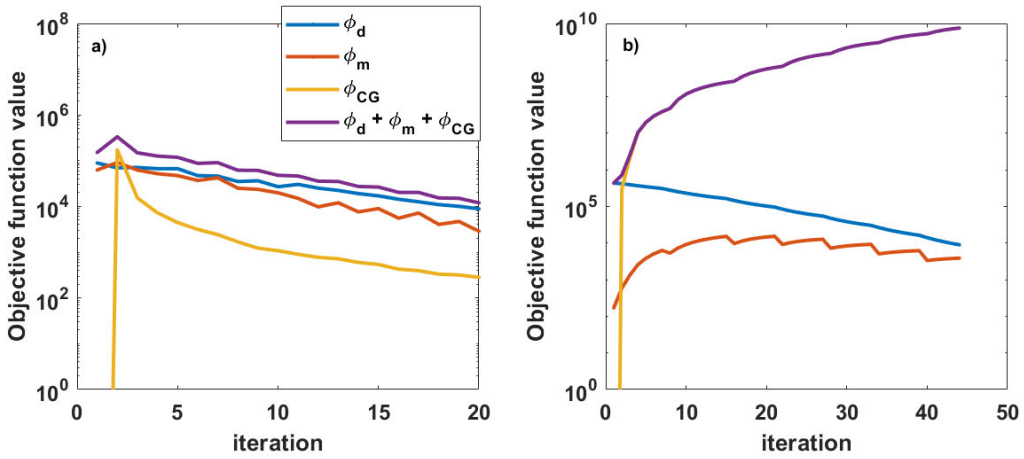

Figure 6. Different components of the objective function for each iteration of the joint inversion with λ=1e7 (a) and λ=1e9 (b). For λ=1e7, the cross-gradient term is small compared to the model and data terms. For λ=1e9, the cross-gradient term is large compared to the model and data terms.

The independent and jointly inverted ERT results all have χ^2 values of ~1. This means that the data fits for each of the models are statistically indistinguishable. However, they show slightly different structures. For example, the independently inverted result shows a trough-like structure between 1000 and 2000 m. This structure is still apparent, although it is not as resistive, in the λ=1e7 joint inversion result and doesn't exist at all in the λ=1e9 jointly inverted result. For the λ=1e9 joint result, conductivity variations below an elevation of ~120 m appear to be driven by the smoothing of two relatively shallow conductive bodies.

Given the dissimilarities between the two jointly inverted ERT results (Figure 4b and d) and their similar data misfit statistics, it can be concluded that for this dataset, the cross-gradient constrained joint inversion does not improve the joint interpretability of the inverted geophysical images. Further, it can be seen that above around 125 m elevation, both of the jointly inverted results and independent inversion results show very similar structure. The major differences occur at lower elevations (greater depths), suggesting the ERT data is not sensitive to structures at elevations lower than 50-100 m, as indicated by the normalized sensitivity shading.

5.0 Conclusions

This report describes the results of a structurally constrained, joint inversion of seismic refraction and ERT data using E4D. The data chosen for this analysis were coincident seismic and ERT profiles obtained between the 200 Areas of Hanford to investigate an inferred hydraulic connection between the 200 East and West areas. Previously, the datasets were inverted separately, and it was observed that the different methods produced structurally similar results. Each of the models broadly indicated a layered system with a trough-like structure. However, the seismic image suggests that the boundary between the two layers is not as deep as the ERT image suggests.

It was anticipated that the joint-inversion approach would lead to models that were more readily interpretable in terms of the stratigraphic structure between the 200 Areas. In this area, there are few boreholes and there is limited knowledge about the stratigraphic structure. The results of the joint inversion indicate that because the seismic structure has very small and predominantly vertical gradients in most of the model domain and the ERT gradients are also predominantly vertical (i.e. parallel to the seismic structure at most locations), the cross-gradient term in the joint inversion has a relatively small impact on the ERT structure unless the λ value is chosen to be very high. In that case, the joint inversion had a large impact on the ERT result, but the cross-gradient term continued to increase throughout the inversion, indicating that the ERT and seismic models became less and less structurally similar at each iteration.

Other avenues to improve the joint interpretability of seismic refraction and ERT data on the Hanford Site include the following:

1. A systematic investigation of model resolution. ERT sensitivity tends to smoothly decrease with depth, whereas seismic resolution tends to be patchy, especially for regions with low seismic gradients like the suprabasalt sediments in the Hanford Site subsurface. Better constraints on what parts of the inverted images are well resolved will improve interpretations. For example, knowledge of what parts of the inverted images are truly sensitive to the data fit will improve interpretation of deeper structure. This could be done, for example, through a global optimization procedure in which a large number of candidate models are generated from which statistics on each of the model parameters may be generated. Such an approach would be computationally expensive.

2. An investigation into the physical parameters that are driving the ERT response. Seismic and ERT measurements are not always sensitive to the same physical properties, and other joint inversion strategies exist where the models are linked through petrophysical parameters instead of structural parameters. Such an investigation would require downhole seismic and ERT measurements along with core analysis. The surface geophysical results could be matched with the downhole measurements and tied to lithological interpretations and petrophysical measurements on the core. Currently, such data does not exist for this area but could allow for a more robust interpretation and contribution to support the GFM refinement and development.

6.0 Quality Assurance

This work was performed in accordance with the Pacific Northwest National Laboratory Nuclear Quality Assurance Program (NQAP). The NQAP complies with DOE Order 414.1D, *Quality Assurance*. The NQAP uses NQA-1-2012, *Quality Assurance Requirements for Nuclear Facility Application,* as its consensus standard and NQA-1-2012, Subpart 4.2.1, as the basis for its graded approach to quality.

This work emphasized acquiring new theoretical or experimental knowledge. The information associated with this report should not be used as design input or operating parameters without additional qualification and should be considered For Information Only (FIO).

7.0 References

Archie, G. E. 1942. “The Electrical Resistivity Log as an Aid in Determining Some Reservoir Characteristics.” *Petroleum Transactions of AIME* 146: 54-62.

Binley, A., and L. Slater. 2020. *Resistivity and Induced Polarization: Theory and Applications to the near-Surface Earth. Cambridge University Press*.

Dijkstra, E. W. 1959. “A Note on Two Problems in Connexion with Graphs.” *Numerische Mathematik* 1: 269-271.

Haber, E., and D. Oldenburg. 1997. “Joint Inversion: A Structural Approach.” *Inverse Problems* 13: 63-77.

Hyde, E. R., M. A. Speece, C. A. Link, T. R. Repasky, M. D. Thompson, and S. F. Miller. 2011. “A Seismic Landstreamer Survey at the Hanford Site, Washington, U.S.A.” *Environmental and Engineering Geoscience* 17: 227-239. https://doi.org/10.2113/gseegeosci.17.3.227.

Johnson, T. C. 2014. *E4d : A Distributed Memory Parallel Electrical Geophysical Modeling and Inversion Code User Guide - Version 1.0.* Pacific Northwest National Laboratory, Richland, WA.

Johnson, T. C., R. J. Versteeg, A. Ward, F. D. Day-Lewis, and A. Revil. 2010. “Improved Hydrogeophysical Characterization and Monitoring through Parallel Modeling and Inversion of Time-Domain Resistivity and Induced-Polarization Data.” *Geophysics* 75 (4).

Johnson, T. C., and D. Wellman. 2015. “Accurate Modelling and Inversion of Electrical Resistivity Data in the Presence of Metallic Infrastructure with Known Location and Dimension.” *Geophysical Journal International* 202 (2): 1096-1108. https://doi.org/10.1093/gji/ggv206.

Jordi, C. 2020. “Structurally Coupled Joint Inversion on Irregular Meshes.” Doctoral, ETH Zurich, ETH Zurich.

Linneman, D. C., C. E. Strickland, and A. R. Mangel. 2021. “Compressional Wave Velocity and Effective Stress in Unsaturated Soil: Potential Application for Monitoring Moisture Conditions in Vadose Zone Sediments.” *Vadose Zone Journal* 20 (5). https://doi.org/10.1002/vzj2.20143.

Moser, T. C. 1991. “Shortest Path Calculation of Seismic Rays.” *Geophysics* 56 (1): 59-67.

Redpath, B. B. 2007. *Downhole Measurements of Shear- and Compression-Wave Velocities in Boreholes C4993, C4996, C4997 and C4998 at the Waste Treatment Plant Doe Hanford Site.* Pacific Northwest National Laboratory, PNNL-16559. Richland, WA (United States).

Robinson, J., J. St. Clair, J. Thomle, P. Jaysaval, J. Cambeiro, K. Peta, F. Day-Lewis, and R. D. Mackley. 2023. “Using Multiple Geophysical Methods to Refine a Stratigraphic Conceptual Site Model at a Nuclear Waste Site.” *Environmental Processes* 10 (1). https://doi.org/10.1007/s40710-023-00622-1.

Robinson, J., J. Thomle, D. McFarland, K. Deters, M. Rockhold, F. Day-Lewis, and V. Freedman. 2022. “Integration of Large-Scale Electrical Imaging into Geological Framework Development and Refinement.” *Environmental Processes* 9 (2). https://doi.org/10.1007/s40710-022-00570-2.

Robinson, J. L., R. D. Mackley, M. L. Rockhold, T. C. Johnson, J. N. Thomle, C. D. Johnson, and P. Jaysaval. 2020. *Geophysical Methods for Stratigraphic Identification.* Pacific Northwest National Laboratory, PNNL-29182, Rev. 1.0. Richland, WA.

Rohay, A. C., and T. M. Brouns. 2007. *Site-Specific Velocity and Density Model for the Waste Treatment Plant, Hanford, Washington.* Pacific Northwest National Laboratory, PNNL-16652. Richland, WA (United States).

St. Clair, J. 2015. "Geophysical Investigations of Underplating at the Middle American Trench, Weathering in the Critical Zone, and Snow Water Equivalent in Seasonal Snow." Doctoral thesis submitted at University of Wyoming.

St. Clair, J. T., A. R. Mangel, and T. C. Johnson. 2023. "New Insights from Legacy Seismic Data Regarding Basalt Elevations and Variability on the Hanford Site." *Environmental and Engineering Geoscience* XXIX (2): 93-104.

Zhu, Y., T. Johnson, and F. Zhang. 2020. *A New Capability of E4d for 3d Parallel Joint Inversion of Dc Resistivity and Traveltime Data on Unstructured Mesh.* Pacific Northwest National Laboratory, PNNL-29966. Richland, WA.

Pacific Northwest National Laboratory

902 Battelle Boulevard
P.O. Box 999
Richland, WA 99354
1-888-375-PNNL (7665)

www.pnnl.gov